Supporting information

Synergistic redox enhancement in ternary Mn–ZnFeOOH oxyhydroxides for high-performance supercapacitor applications

Palanisamy Rajkumar[a], Vediyappan Thirumal[a], Neela Mohan Chidambaram[b], Maalavika S Iyer[c], Murugesan Prasanna[d], Ingyung Park[f], Soo-Hyun Kim[e,f,*], Kisoo Yoo[a,*], Jinho Kim[a,*]

[a] Department of Mechanical Engineering, Yeungnam University, Gyeongsan-si, Gyeongbuk-do 38541, Republic of Korea

[b] Department of Chemistry, Srimad Andavan Arts and Science College (Autonomous), Affiliated to Bharathidasan University, Tiruchirappalli, Tamil Nadu 620005, India

[c] SSN Research Centre, Sri Sivasubramaniya Nadar College of Engineering, Kalavakkam, Chennai 603110 Tamil Nadu, India

[d] Graduate School of Advanced Science and Technology, Japan Advanced Institute of Science and Technology, 1-1 Asahidai, Nomi, Ishikawa 923-1292, Japan

[e] Graduate School of Semiconductor Materials and Devices Engineering, Ulsan National Institute of Science and Technology (UNIST), Ulju-gun, Ulsan 44919, Republic of Korea

[f] Department of Materials Science and Engineering, Ulsan National Institute of Science and Technology (UNIST), Ulju-gun, Ulsan 44919, Republic of Korea

Corresponding Authors: soohyunsq@unist.ac.kr (SK), kisooyoo@ynu.ac.kr (KY), jinho@ynu.ac.kr (JK)

Electrochemical Study:

Preparation of electrodes: Electrochemical performance was systematically evaluated through cyclic voltammetry (CV), galvanostatic charge–discharge (GCD) and electrochemical impedance spectroscopy (EIS) to assess the charge storage behavior, rate capability and resistance characteristics of the fabricated electrodes. Measurements were carried out in a conventional three-electrode cell configuration, employing Ag/AgCl as the reference electrode, a platinum wire as the counter electrode and the prepared material-coated Ni-foam as the working electrode. The working electrodes were fabricated via the doctor blade technique. Specifically, the active material, Super P conductive carbon and polyvinylidene fluoride (PVDF) binder were homogenously mixed in a weight ratio of 80:10:10 using N-methyl-2-pyrrolidone (NMP) as the dispersing solvent to obtain a uniform slurry. The resultant slurry was uniformly spread onto pre-cleaned Ni-foam substrates and subsequently dried in a vacuum oven at 60 °C for 8 h to ensure complete removal of residual solvent and proper adhesion of the coating. After drying, the electrodes were pressed lightly to enhance contact between the active material and the current collector. Aqueous 3 M KOH solution served as the electrolyte for all electrochemical evaluations.

For practical device fabrication, an asymmetric coin-cell supercapacitor was assembled using the electrode material as positive and carbon black (CB) as negative electrode. The preparation of electrodes was done as discussed above. Whattmann filter paper wetted with 3M KOH solution was used as separator and was placed between the two electrodes. The electrodes were balanced according to the charge-balance principle $q^+ = q^-$. The required mass ratio of positive and negative electrodes is:

$$\frac{m^+}{m^-} = \frac{C_{sp}^- \Delta V^-}{C_{sp}^+ \Delta V^+} \qquad \text{(Eq. 1)}$$

Where, $C^{+/-}_{sp}$ - capacitance of each electrode obtained from three electrode system. $\Delta V^{+/-}$ - potential window used for each electrode. $m^{+/-}$ - mass of active material on each electrode.

Capacitance Evaluation: The following equation is used to determine the specific capacitance of the electrode from cyclic voltammetry graph:

$$C_{sp} = \frac{\int I\, dv}{2mv\Delta V} \qquad \text{(Eq. 2)}$$

Here, *I* represent the current, *v* denotes the scan rate, m corresponds to the integrated area under the CV curve, $\triangle$V indicates the applied potential window.

The specific capacitance of the electrode was evaluated from the Galvanostatic Charge Discharge plot using the equation:

$$C_{sp} = \frac{I \times \Delta t}{\Delta V \times m} \qquad \text{(Eq.3)}$$

where *I* - applied discharge current, Δt - discharge time, ΔV - potential window and *m* - mass of the electroactive material (optimized to 1 mg) coated on the current collector.

The CV and GCD measurements were carried out at scan rates of 10, 20, 40, 60, 80 and 100 mV s^{-1} and at current densities of 1, 2, 3, 5 and 10 A g^{-1}, respectively, to evaluate the rate capability and charge storage behavior of the electrode. EIS was performed in the frequency range of 10^5 to 0.01 Hz with an applied AC perturbation of 5 mV amplitude. All electrochemical experiments were conducted under ambient room temperature conditions.

Efficiency Evaluation: For the asymmetric supercapacitor device, the energy and power density were calculated using the following formula:

$$E = \frac{C_{sp}}{2 \times 3.6} \times \Delta V^2 \qquad \text{(Eq.4)}$$

$$P = \frac{E}{\Delta t} \times 3600 \quad \text{(Eq.5)}$$

Where C_{sp} is the specific capacitance obtained, ΔV is the potential window, Δt is the discharge time from the GCD profile.

Charge storage mechanism: Power-law model is used to analyse the reduction and oxidation reactions of FZMn-15 electrode.

$$i_p = a \times v^b \quad \text{(Eq.6)}$$

Here, i_p denotes the peak current (A), v represents the scan rate (V s^{-1}), a is a constant and b is the exponential factor that indicates the charge storage mechanism.

The modified power law was employed to deconvolute the relative contributions of diffusion-controlled and capacitive-controlled processes occurring at the electrode/electrolyte interface. The relationship is expressed by the following equation:

$$i_p = k_1 v + k_2 v^{1/2} \quad \text{(Eq.7)}$$

$$i_p / v^{1/2} = k_1 v^{1/2} + k_2 \quad \text{(Eq.8)}$$

The overall current response i_p is the sum of two contributions: the diffusion-controlled process $k_2 v^{1/2}$ and the capacitive-controlled process $k_1 v$.

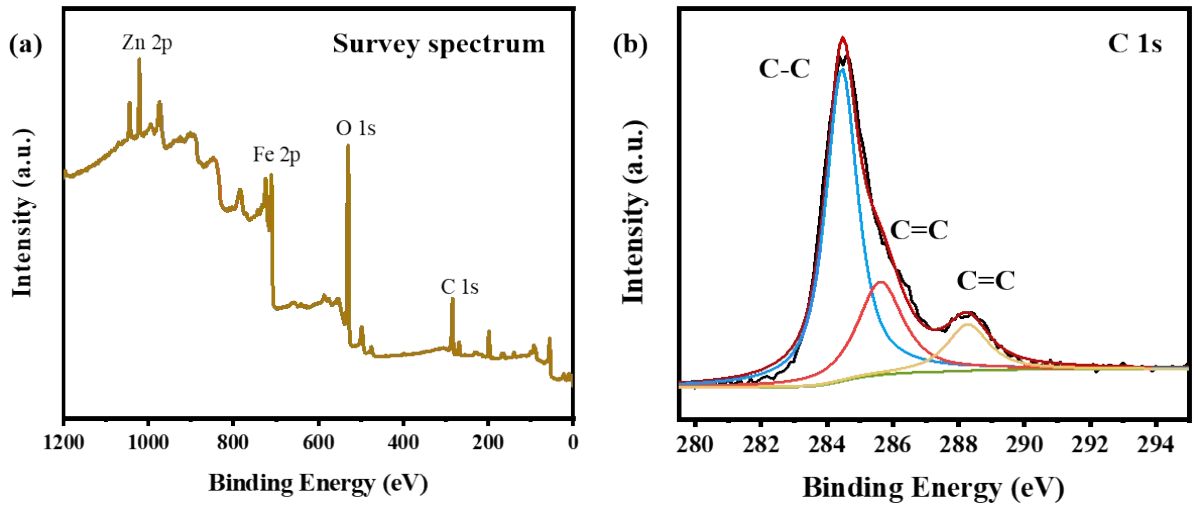

Figure S1: (a) XPS survey spectrum and **(b)** deconvoluted C 1s spectra of the FZMn-15 sample

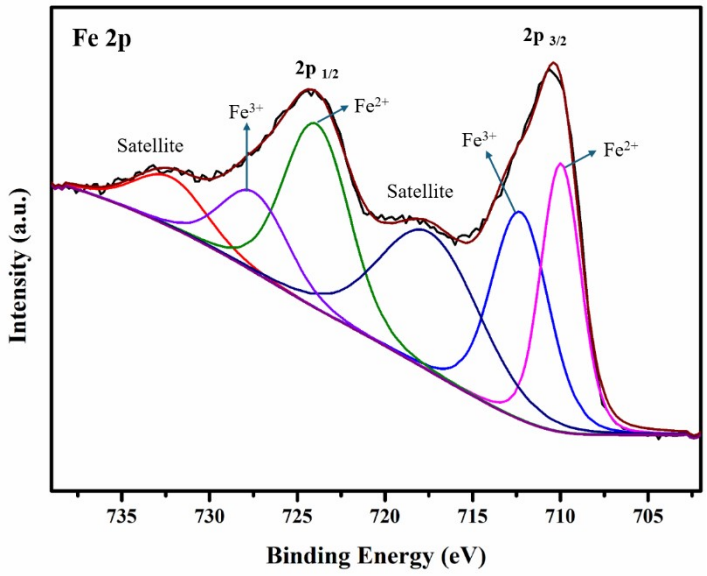

Figure S2: Deconvoluted Fe 2p spectra of the FeOOH sample

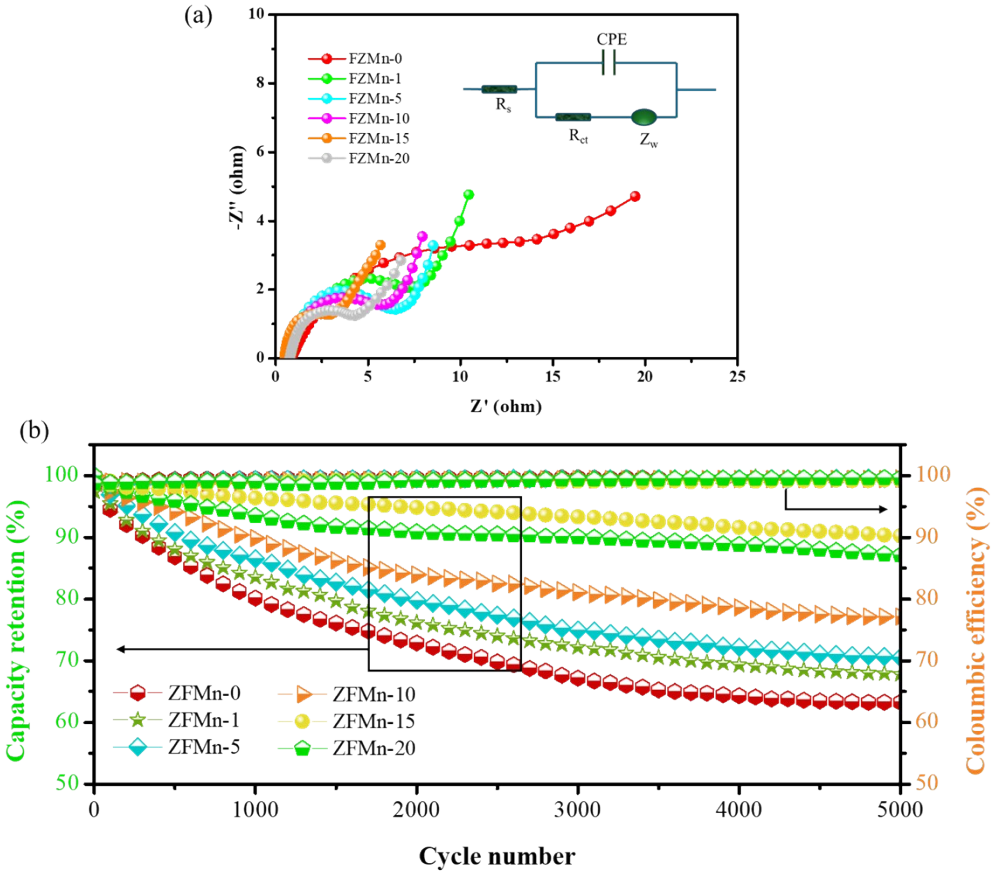

Figure S3: (a) EIS spectra (inset: equivalent circuit) and (b) long-term cycling stability of the FZMn-15 electrode in three electrode system

Cycling stability:

Figure S2b depicts the long-term cycling stability of all the prepared electrodes over 5000 charge/discharge cycles. The decreased capacitance retention of 63% for FZMn–0 and 67% for FZMn–1 can be seen (Figure S2b), which may be attributed to their poor electrical conductivity and limited electroactive surface area. These factors lead to higher internal resistance and sluggish ion diffusion during repeated charge–discharge processes, resulting in rapid fading of coulombic efficiency. In the stability plots of FZMn–5, FZMn–10, and FZMn–20, the capacitance retention found to be 70%, 77%, and 87%, respectively. This gradual decrease can be ascribed to structural degradation of the electrode material, partial agglomeration of Mn species at higher loadings, and loss of electrochemically active sites during prolonged cycling. While FZMn–5 and FZMn–10 show moderate retention, indicating reasonably stable electrode–electrolyte interfaces, the relatively better retention in FZMn–20 suggests that although excessive Mn incorporation increases initial capacitance, it also partially blocks ion transport pathways, leading to capacitance loss over long-term cycling. Among the series, FZMn–15 exhibited outstanding performance, retaining a high percentage of its initial capacitance even after extended cycling, along with nearly 100% coulombic efficiency, confirming excellent reversibility. FZMn–15 demonstrates exceptional long-term cycling stability, maintaining 90% of its initial capacitance even after 5000 continuous charge–discharge cycles. This remarkable retention highlights the robustness of the electrode structure, which effectively withstands repeated ion intercalation and deintercalation without undergoing significant degradation or loss of active sites.

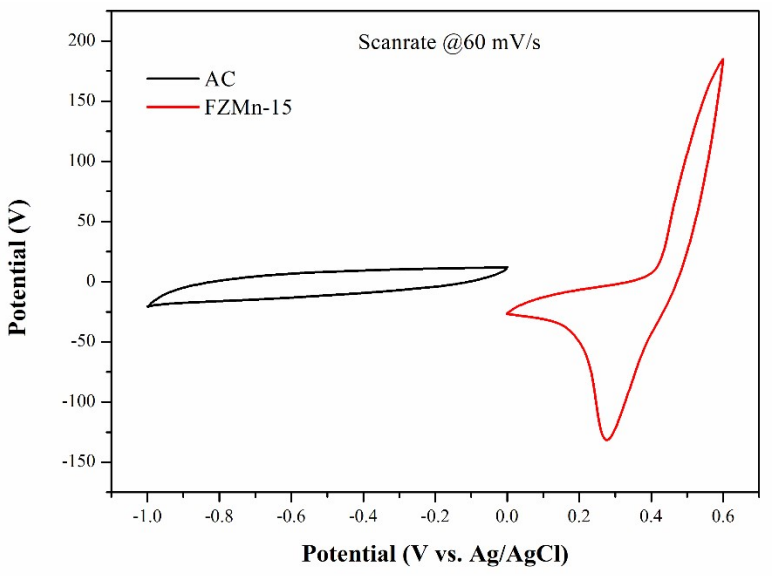

Figure S4: Comparison CV curve of Activated carbon and FZMn-15 electrode in the three-electrode system

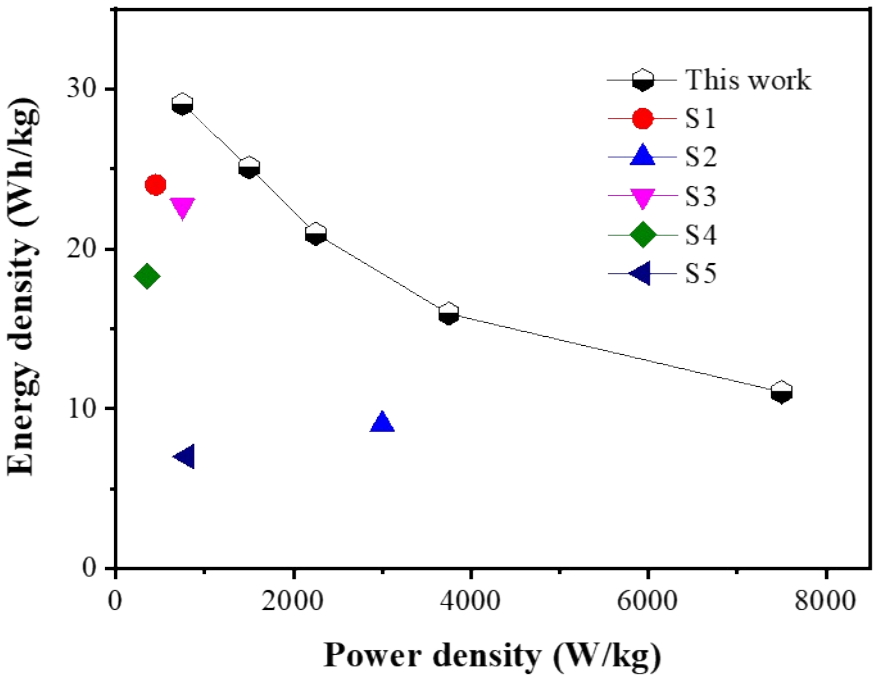

Figure S5: Ragone plot of the FZMn-15 electrode with previously reported results

Figure S5 shows the post-cycling X-Ray Diffraction studies of FZMn-15@Ni-Foam. The dominant diffraction peaks marked as # belongs to Ni foam. the absence of sharp peaks suggests the absence of bulk phase transformation during cycling. The inset image shows the peaks in the range 20° to 60°, the weak and broad peaks observed in this range can be attributed to FZMn-15 sample. The broadness of the peaks indicates that the sample has turned partially amorphous due to repeated cycling, which is typical for electrochemically reconstructed oxyhydroxide-type phases. The post-cycling XRD indicates that the electrode maintains the structural integrity, while the active phase might have undergone surface reconstruction rather than forming a new crystalline phase.

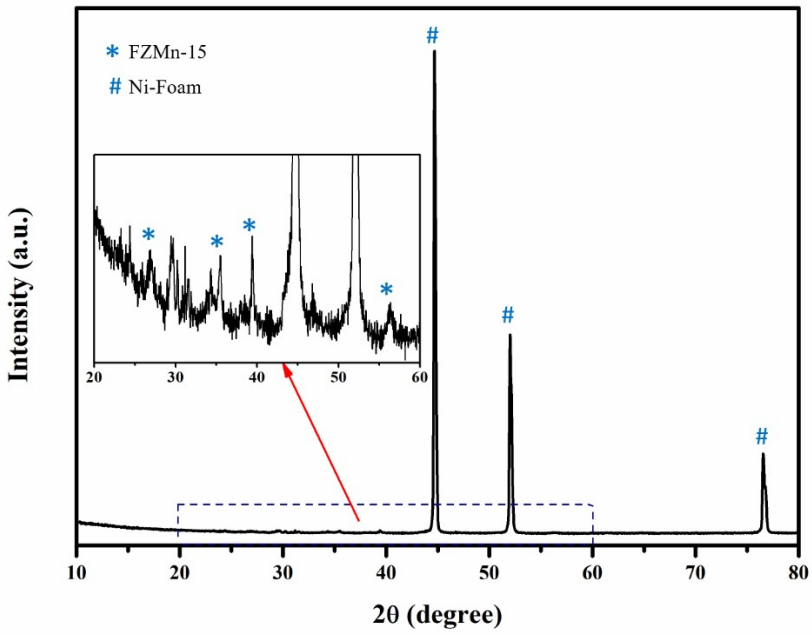

Figure S6: XRD spectra of after cycling FZMn-15 electrode

Figure S6 shows the Scanning Electron Microscopic images of FZMn-15 sample post-cycling. The SEM image shows the electrode surface with aggregations and the absence of pronounced grains, which indicates that the material has undergone electrochemical surface reconstruction as suggested by XRD. At higher magnification, the structure appears more porous with loosely packed nanograins, indicating partial amorphization or formation of an oxyhydroxide layer. No

major cracks or delamination are observed, confirming that the electrode retains structural integrity after cycling.

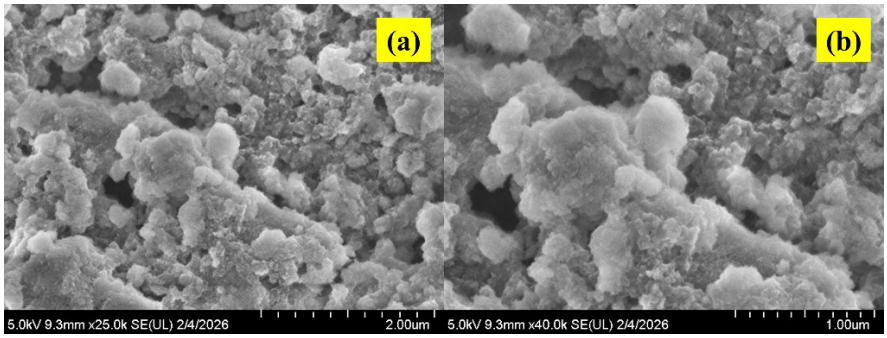

Figure S7: SEM image of FZMn-15 post cycling.

Table S1: Comparison of the electrochemical performance of the present work with previously reported results in a three-electrode system

S.No.	Electrode Material	Electrolyte	Current Density (A/g)	Specific Capacitance (F/g)	Ref.
1	(Ni,Co)OOH/CNTs	2 M KOH	1	460	[S6]
2	MnOOH/GF	1 M $LiClO_4$/PC	1	1156	[S7]
3	EA-CoOOH	6 M KOH	1	832	[S8]
4	NCM/CC	6 M KOH	3	707	[S9]
5	CNTs/α-MnOOH	0.1 M Na_2SO_4	0.65	202	[S10]
6	MnOOH/graphene	6 M KOH	0.5	268	[S11]
7	CoOOH	3 M KOH	0.1	198	[S12]
8	$VO_x(OH)_y$/CNT/rGO	1 M $LiClO_4$/PC	0.5	414	[S13]
9	FeOOH QDs/FGS	1 M Li_2SO_4	1	365	[S14]
10	FeOOH	2 M KOH	1	1066	[S15]
11	α-FeOOH	1 M Na_2SO_4	1	224.6	[S16]
12	FeOOH@MWCNT	0.5 M Na_2SO_4	1	345	[S17]
13	FeOOH@Gr	2 M KOH	3	1150.3	[S18]
14	FeOOH/MnO_2	1 M Na_2SO_4	0.5	350.2	[S19]
15	FZMn–15	3 M KOH	1	1531	This work

Table S2: Comparison of the electrochemical performance of the FZMn–15||AC device with previously reported results

S.No.	Device	Electrolyte	Current Density (A/g)	Specific Capacitance (F/g)	Ref.
1	$Ni_{60}Co_{40}$ 600//AC	1 M KOH	1	42	[S20]
2	FeOOH//MnO_2	1 M Li_2SO_4	0.5	51	[S21]
3	MnO2@SBA-C//FeOOH@SBA-C	1 M Na_2SO_4	0.5	70.9	[S22]
4	MnOOH/NiAl-LDH//AC	6 M KOH	1	75.63	[S23]
5	MnOOH/CC//AC	0.5 M $LiNO_3$	1	81.1	[S24]
6	MnOOH/3D-rGO//AC	1 M Na_2SO_4	0.8	96.1	[S25]
7	FZMn–15||AC	3 M KOH	1	92	This work

Reference:

[S1]. Jin, W.H., Cao, G.T. and Sun, J.Y., 2008. Hybrid supercapacitor based on MnO_2 and columned FeOOH using Li_2SO_4 electrolyte solution. *Journal of Power Sources, 175(1),* pp.686-691.

[S2]. Karthikeyan, K., Kalpana, D., Amaresh, S. and Lee, Y.S., 2012. Microwave synthesis of graphene/magnetite composite electrode material for symmetric supercapacitor with superior rate performance. *RSC Advances, 2(32),* pp.12322-12328.

[S3]. Sun, Q., Yao, K. and Zhang, Y., 2020. MnO_2-directed synthesis of NiFe-LDH@ FeOOH nanosheeet arrays for supercapacitor negative electrode. *Chinese Chemical Letters, 31(9),* pp.2343-2346.

[S4]. Fan, H., Niu, R., Duan, J., Liu, W. and Shen, W., 2016. Fe_3O_4@ carbon nanosheets for all-solid-state supercapacitor electrodes. *ACS applied materials & interfaces, 8(30),* pp.19475-19483.

[S5]. Raj, C.J., Kim, B.C., Cho, W.J., Park, S., Jeong, H.T., Yoo, K. and Yu, K.H., 2015. Rapid hydrothermal synthesis of cobalt oxyhydroxide nanorods for supercapacitor applications. *Journal of Electroanalytical Chemistry, 747,* pp.130-135.

[S6]. Li, M., Cheng, J.P., Liu, F. and Zhang, X.B., 2015. In situ growth of nickel-cobalt oxyhydroxide/oxide on carbon nanotubes for high performance supercapacitors. Electrochimica Acta, 178, pp.439-446.

[S7]. Tan, H.T., Rui, X., Shi, W., Xu, C., Yu, H., Hoster, H.E. and Yan, Q., 2013. Controlled Synthesis of Manganese Oxyhydroxide Nanotubes: Implications for High-Efficiency Supercapacitors. ChemPlusChem, 78(6), pp.554-560.

[S8]. Guo, W., Yu, C., Li, S., Song, X., Huang, H., Han, X., Wang, Z., Liu, Z., Yu, J., Tan, X. and Qiu, J., 2019. A universal converse voltage process for triggering transition metal hybrids in situ phase restruction toward ultrahigh-rate supercapacitors. Advanced Materials, 31(28), p.1901241.

[S9]. Nath, A.R., Jayachandran, A. and Sandhyarani, N., 2019. Nanosheets of nickel, cobalt and manganese triple hydroxides/oxyhydroxides as efficient electrode materials for asymmetrical supercapacitors. Dalton Transactions, 48(13), pp.4211-4217.

[S10]. H. Fang, S. Zhang, X. Wu, W. Liu, B. Wen, Z. Du, and T. Jiang, *Journal of Power Sources*, 2013, **235**, 95-104.

[S11]. Y. Cao, Y. Xiao, Y. Gong, C. Wang, and F. Li, *Electrochimica Acta*, 2014, **127**, 200-207.

[S12]. C.J. Raj, B.C. Kim, W.J. Cho, S. Park, H.T. Jeong, K. Yoo, and K.H. Yu, *Journal of Electroanalytical Chemistry*, 2015, **747**, 130-135.

[S13]. M. Chen, Y. Zhang, Y. Liu, Q. Wang, J. Zheng, and C. Meng, *ACS Applied Energy Materials*, 2018, **1(10)**, 5527-5538.

[S14]. J. Liu, M. Zheng, X. Shi, H. Zeng, and H. Xia, *Advanced Functional Materials*, 2016, **26(6)**, 919-930.

[S15]. K.A. Owusu, L. Qu, J. Li, Z. Wang, K. Zhao, C. Yang, K.M. Hercule, C. Lin, C. Shi, Q. Wei, and L. Zhou, *Nature Communications*, 2017, **8(1)**, 14264.

[S16]. K. Li, X. Liu, T. Zheng, D. Jiang, Z. Zhou, C. Liu, X. Zhang, Y. Zhang, and D. Losic, *Chemical Engineering Journal*, 2019, **370**, 136-147.

[S17]. C. Sun, W. Pan, D. Zheng, Y. Zheng, J. Zhu, and C. Liu, *ACS Omega*, 2020, **5(9)**, 4532-4541.

[S18]. N. Li, X. Huang, and H. Zhang, *Journal of Alloys and Compounds*, 2017, **712**, 194-203.

[S19]. Q. Lu, L. Liu, S. Yang, J. Liu, Q. Tian, W. Yao, Q. Xue, M. Li, and W. Wu, *Journal of Power Sources*, 2017, **361**, 31-38.

[S20]. A. Roy, H.R. Inta, S. Ghosh, H.V. Koppisetti, A. Mondal, B.R. Verma, S. Bag, and V. Mahalingam, *Journal of Materials Chemistry A*, 2024, **12(7)**, 4086-4098.

[S21]. W.H. Jin, G.T. Cao, and J.Y. Sun, *Journal of Power Sources*, 2008, **175(1)**, 686-691.

[S22]. Y. Chen, C. Jing, X. Fu, M. Shen, T. Cao, W. Huo, X. Liu, H.C. Yao, Y. Zhang, and K.X. Yao, *Applied Surface Science*, 2020, **503**, 144123.

[S23]. X. Hua, C.J. Mao, J.S. Chen, P.P. Chen, and C.F. Zhang, *Journal of Alloys and Compounds*, 2019, **777**, 749-758.

[S24]. Y. Zhang, Z. Hu, Y. An, B. Guo, N. An, Y. Liang, and H. Wu, *Journal of Power Sources*, 2016, **311**, 121-129.

[S25]. S. Sun, S. Wang, T. Xia, X. Li, Q. Jin, Q. Wu, L. Wang, Z. Wei, and P. Wang, *Journal of Materials Chemistry A*, 2015, **3(42)**, 20944-20951.